

**Structural systematics in the isomorphous binary co-crystal solvates comprising 2,2'-dithiodibenzoic acid, 4-halobenzoic acid and dimethylformamide (1:1:1), for halide = chloride, bromide and iodide†**

Sang Loon Tan, Kong Mun Lo, Yee Seng Tan and Edward R. T. Tiekink\*

Research Centre for Crystalline Materials, School of Medical and Life Sciences, Sunway University, 47500 Bandar Sunway, Selangor Darul Ehsan, Malaysia

E-mail: [edwardt@sunway.edu.my](mailto:edwardt@sunway.edu.my) (ERTT)

ORCID ID: 0000-0002-5343-3382 (SLT); 0000-0001-7500-8734 (KML); 0000-0002-0144-3298 (TYS); 0000-0003-1401-1520 (ERTT)

**Abstract**

The 1:1:1 binary co-crystal solvates formulated as 2,2'-dithiodibenzoic acid (DTBA), 4-halobenzoic acid (4-XBA) and dimethylformamide (DMF) for X = Cl (**1**), Br (**2**) and I (**3**) are isomorphous and the supramolecular association in this series has been probed by a wide range of computational chemistry techniques. The common feature of the molecular packing is the formation of robust three-molecule aggregates sustained by a non-symmetric  $\{\cdots\text{HOC}=\text{O}\}_2$  synthon, formed between DTBA and 4-XBA, and a DTBA-hydroxyl-O-H $\cdots$ O(carbonyl-DMF) hydrogen bond (with a reciprocating DMF-C-H $\cdots$ O(carbonyl-DTBA) contact). Supramolecular tapes are evident and feature DTBA-C-H $\cdots$ O(DMF), DTBA-C-H $\cdots$ S(DTBA), DMF-O $\cdots$  $\pi$ (DTBA-phenyl) and DMF-C-H $\cdots$  $\pi$ (DTBA-phenyl) contacts. The point-to-point connections between tapes are of the type  $\pi$ (4-XBA-phenyl) $\cdots$  $\pi$ (DTBA-phenyl),  $\pi$ (4-XBA-phenyl) $\cdots$  $\pi$ (4-XBA-phenyl), DTBA-C-H $\cdots$  $\pi$ (DTBA-phenyl) and DMF-C $\cdots$ X

tetrel bonding. However, a difference is noted here between **1** and **2**, and **3**, in that the DTBA-C–H $\cdots\pi$ (DTBA-phenyl) contacts are beyond standard separations, a feature of the packing that is traced directly to the influence of the iodide atom as opposed to the lighter congeners. There are systematic increases in the *b* and *c* unit-cell lengths correlating with the size of the halide and in the case of **3** this expansion diminishes the influence of the DMF-C–H $\cdots\pi$ (DTBA-phenyl) contact as the tapes are pushed apart. This contact along the *a*-direction in **3** is replaced by DMF-H $\cdots$ O(DTBA-carbonyl) and DTBA-C–H $\cdots$ S(DTBA) contacts. Additional attractive interactions along the *a*-axis include C–X $\cdots$ quasi- $\pi$ [ $\{\cdots\text{HOC}=\text{O}\}_2$ ] bonding interactions which are at a maximum strength in **3** (*ca* 5.0 kJ/mol) and contribute to the shortening of the *a*-axis in the order **3** < **2** < **1**.

### Footnote

† Electronic supplementary information (ESI) available: Tables of intra- and inter-molecular parameters, experimental and calculated PXRD patterns, TGA thermograms, DSC traces, thermo-microscopic images, molecular and packing diagrams, MEP diagrams, isostructurality dendrogram, NCI plots, energy frameworks and Hirshfeld surface  $d_{\text{norm}}$ -mappings, curvedness, shape index and two-dimensional fingerprint plots. CCDC 2142263-2142265 contain the supplementary crystallographic data for this paper. For ESI and crystallographic data in CIF or other electronic format see DOI: 10.1039/d0cexxxxxx

### Introduction

The exploration of multi-component crystals, encompassing co-crystal technology, is a key element of crystal engineering and offers many opportunities for practical applications, none the least, related to the pharmaceutical industry.<sup>1-3</sup> The rational assembly of dissimilar

molecules in crystals relies on the control of the supramolecular mode of association between the different entities, among which hydrogen bonding, with clearly enunciated rules for their formation long-established,<sup>4</sup> is prominent through the exploitation of the elegant supramolecular synthon approach.<sup>5</sup> Co-crystal formation *via* hydrogen bonding interactions is the archetype of non-covalent derivatisation of Active Pharmaceutical Ingredients (API's),<sup>6,7</sup> and in this context, carboxylic acids are particularly prevalent.<sup>8</sup> While it may be anticipated the eight-membered homosynthon,  $\{\cdots\text{HOC}=\text{O}\}_2$ , (I) in Fig. 1, might prevail in the crystals of carboxylic acids, this in fact is not the case, with an early review indicating only a 33% adoption rate.<sup>9</sup> For example, in the presence of pyridyl groups, the seven-membered heterosynthon,  $\{\cdots\text{HCN}\cdots\text{HOC}=\text{O}\}$ , (II) in Fig. 1, featuring a hydroxyl-O–H $\cdots$ N(pyridyl) hydrogen bond and supporting C–H $\cdots$ O(carbonyl) interaction, proves persistent,<sup>8</sup> rather than the cyclic synthon. Recent studies<sup>10-12</sup> have shown an analogous seven-membered heterosynthon,  $\{\cdots\text{HC}=\text{O}\cdots\text{HOC}=\text{O}\}$ , (III) in Fig. 1, featuring a hydroxyl-O–H $\cdots$ O(DMF) hydrogen bond and supporting DMF-C–H $\cdots$ O(carbonyl) interaction, can occur in multicomponent crystals of 2,2'-dithiodibenzoic acid (systematic name: 2-[(2-carboxyphenyl)-disulfanyl]benzoic acid), (2-HO<sub>2</sub>C)C<sub>6</sub>H<sub>4</sub>S–SC<sub>6</sub>H<sub>4</sub>(CO<sub>2</sub>H-2), hereafter DTBA, with dimethylformamide (DMF); chemical diagrams for the molecules investigated herein are shown in Fig. 1.

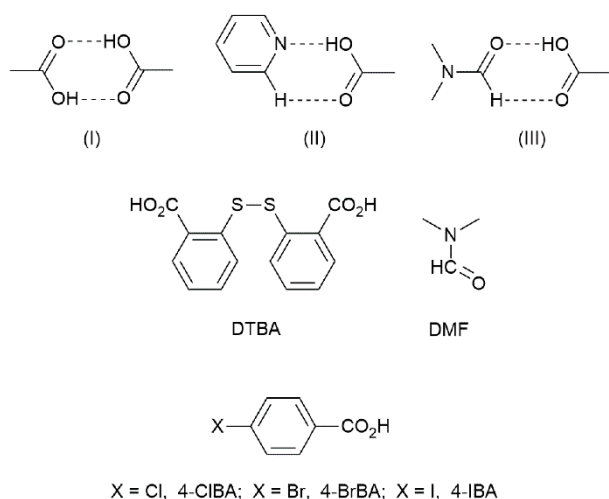


**Fig. 1** (I)-(III) shown representations of synthons discussed herein. Chemical diagrams of the molecules forming the focus of the present study and their abbreviations are also shown.

Co-crystallisation studies have shown DTBA often forms as a result of the *in situ* oxidation of 2-mercaptobenzoic acid (2-MBA).<sup>13-15</sup> In accord with expectation, when DTBA is co-crystallised with molecules bearing two pyridyl residues, the aforementioned seven-membered heterosynthon,  $\{\cdots\text{HCN}\cdots\text{HOC}=\text{O}\}$  is observed leading to supramolecular chains<sup>13,14,16</sup> or oligomers.<sup>17</sup> More variable co-crystallisation outcomes are noted when DTBA occurs in co-crystals of other carboxylic acids. Thus, the 1:1 co-crystallisation (DMF/toluene) of 2-MBA with benzoic acid (BA) gives rise to the anticipated three-molecule aggregate,  $\text{BA}\cdots\text{DTBA}\cdots\text{BA}$ , mediated by dissymmetric  $\{\cdots\text{HOC}=\text{O}\}_2$  synthons.<sup>18</sup> An analogous experiment where BA was substituted by 2-chlorobenzoic acid (2-CIBA) yielded a different three-molecule aggregate formulated as  $2\text{-CIBA}\cdots\text{DTBA}\cdots\text{DMF}$ , featuring one dissymmetric  $\{\cdots\text{HOC}=\text{O}\}_2$  synthon and one  $\{\cdots\text{HC}=\text{O}\cdots\text{HOC}=\text{O}\}$  heterosynthon.<sup>12</sup> When 3-BrBA was employed and toluene was substituted by benzene, a supramolecular chain  $\{\text{DTBA}\}_n$  was formed mediated by symmetric  $\{\cdots\text{HOC}=\text{O}\}_2$  synthons as were centrosymmetric dimers,  $\{3\text{-BrBA}\}_2$ , again mediated by symmetric  $\{\cdots\text{HOC}=\text{O}\}_2$  synthons.<sup>19</sup> A similar outcome was

observed when 3-ClBA was employed and the solvent system was dichloromethane/benzene.<sup>20</sup> It is also noted that crystals of 1:1 DTBA:DMF stoichiometry, give rise to four molecule aggregates, DMF $\cdots$ DTBA $\cdots$ DTBA $\cdots$ DMF,<sup>10</sup> and those of 1:2 DTBA:DMF stoichiometry, give rise to three-molecule aggregates, DMF $\cdots$ DTBA $\cdots$ DMF,<sup>11</sup> again prove the ability of DMF to effectively block  $\{\cdots\text{HOC}=\text{O}\}_2$  synthon formation between DTBA molecules. Indeed, a survey of the Cambridge Structural Database<sup>21</sup> revealed there are approximately 250 structures with lattice DMF and at least one carboxylic acid showed the seven-membered heterosynthon,  $\{\cdots\text{HC}=\text{O}\cdots\text{HOC}=\text{O}\}$  formed in approximately 40% of instances. In continuation of these studies, co-crystallisation experiments of DTBA.DMF<sup>10</sup> with 4-XBA in DMF/toluene (1:2 v/v) yielded the isomorphous series of binary co-crystal solvates<sup>22,23</sup> formulated as 4-XBA $\cdots$ DTBA $\cdots$ DMF, for X = Cl (**1**), Br (**2**) and I (**3**).

The IUCr's Online Dictionary of Crystallography provides precise definitions for isomorphous<sup>24</sup> as opposed to isostructural crystals,<sup>25</sup> with the former relating to the same space group symmetry with closely matched unit-cells, and with chemical composition differing in a relatively minor fashion, such as by a single substituent, e.g. halide.

The control of isostructurality, sometimes referred to the formation of isotypic crystals, offers opportunities in crystal engineering in terms of fine tuning of supramolecular aggregation (strength and directionality),<sup>26-28</sup> but is considered relatively rare except in the case of inclusion compounds.<sup>29,30</sup> In the organic solid-state, such considerations have attracted many systematic studies.<sup>31-44</sup> While these studies have largely focussed upon single-component crystals, increasingly, attention have been directed to evaluating similar phenomena in multi-component crystals.<sup>45-51</sup> Not surprisingly, the majority of the aforementioned studies of both single- and multi-component crystals involve the interchange of halides. The motivation for studying isostructural halide exchange cuts to the core of one of the tenants of crystal engineering,<sup>52</sup> *i.e.* the fine-tuning of solid-state properties, *e.g.* melting point,<sup>53</sup>

luminescence<sup>54</sup> and thermal expansion.<sup>55</sup> With the above in mind, the three isolated binary co-crystal solvates **1-3** have been subjected to a detailed analysis of their molecular packing employing a variety of computational chemistry techniques in order to determine the specific roles of X (= Cl, Br and I) upon the molecular packing within the constraints of an isomorphous series of crystals.

## Experimental

### Chemicals and instrumentation

All chemicals and solvents were used as purchased without purification. The melting points were measured using a Stuart SMP30 melting point apparatus. The CHN elemental analyses were performed on a LECO TruSpec Micro analyser under a helium atmosphere with cystine (Leco) being the standard. The IR spectra were measured on a Bruker Vertex 70v FT-IR spectrophotometer from 4000 to 200  $\text{cm}^{-1}$ . Thermogravimetric analyses (TGA) were performed on a Perkin Elmer STA 6000 Simultaneous Thermogravimetric Analyzer in the range of 25–600 °C under a nitrogen atmosphere at a flow rate of 20 ml/min. The DSC analyses were performed on a PerkinElmer DSC-8000 differential scanning calorimeter in the range of -150 to 80 °C at a rate of 10 °C/min under a helium gas flow. Room temperature powder X-ray diffraction (PXRD) patterns were measured on a Rigaku MiniFlex 600 X-ray diffractometer with Cu  $K\alpha_1$  radiation ( $\lambda = 1.5418 \text{ \AA}$ ) within the  $2\theta$  range 5 to 70° and step size of 0.02°. The comparisons between experimental and calculated (from the respective CIF) PXRD patterns were processed with Rigaku's PDXL2 software (<https://www.rigaku.com/en/products/software/pdxl/overview>). The phase quantification was performed through the Reference Intensity Ratio (RIR) method based upon the scaling of the diffraction data for the mixture with reference to the PXRD patterns obtained for the respective

precursors. The composition of each component present in the mixture was obtained using the following equation:<sup>56</sup>

$$\%X = \frac{I_X \times M_S \times 100}{I_S \times M \times RIR}$$

where  $I_X$  is the intensity of the component  $X$  in the mixture,  $M_S$  is the mass of the precursor,  $I_S$  is the intensity of the chosen reflection of the precursor,  $M$  is the mass of the mixture and  $RIR$  is the reference intensity ratio. Crystals **1-3** were subjected to thermo-microscopic analysis using a Leica DM2700P microscope equipped with a Linkam LTS420 thermal stage connected to a T95 temperature console controlled through the LINK software system. Micrographs of the thermal process were recorded at 20× magnification through a DFC digital camera.

### Preparation of **1-3**

2,2'-Dithiodibenzoic acid (DTBA), as its mono-DMF solvate, was prepared as previously described.<sup>10</sup> The binary co-crystal solvates **1-3** were prepared by mixing DTBA.DMF (0.306 g, 0.001 mol) with the respective 4-halobenzoic acid (X = Cl: Merck, 0.157 g, 0.001 mol; X = Br: Alfa Aesar, 0.201 g, 0.001 mol; X = I: Alfa Aesar, 0.248 g, 0.001 mol) in the presence of three drops of *N,N*-dimethylformamide in a 2.0 ml conical bottom micro-centrifuge tube and then subjected to mechano-grinding using a Retsch CryoMill for two minutes at 30 Hz under ambient conditions. The grinding was repeated twice after one-minute intervals. Colourless crystals were obtained through careful layering of toluene (2 ml) on an *N,N*-dimethylformamide (1 ml) solution of each ground mixture.

**1**: Calcd. for C<sub>24</sub>H<sub>22</sub>ClNO<sub>7</sub>S<sub>2</sub>: C, 53.78; H, 4.14; N, 2.61%. Found: C, 53.61; H, 4.18; N, 2.52%. IR (ATR, cm<sup>-1</sup>): 3093 (m) ν(C–H); 1674 (s) ν(C=O); 1468 (s) ν(C=C); 1417 (m) δ(C–H); 819 (w) ν(C–Cl); 650 (m) ν(C–S); 490 (w) ν(S–S).

**2**: Calcd. for C<sub>24</sub>H<sub>22</sub>BrNO<sub>7</sub>S<sub>2</sub>: C, 49.66; H, 3.82; N, 2.41%. Found: C, 49.51; H, 3.68; N, 2.29%.

IR (ATR, cm<sup>-1</sup>): 3089 (m)  $\nu$ (C–H); 1673 (s)  $\nu$ (C=O); 1469 (s)  $\nu$ (C=C); 1415 (m)  $\delta$ (C–H); 720 (w)  $\nu$ (C–Br); 650 (m)  $\nu$ (C–S); 463 (w)  $\nu$ (S–S).

**3**: Calcd. for C<sub>24</sub>H<sub>22</sub>INO<sub>7</sub>S<sub>2</sub>: C, 45.94; H, 3.53; N, 2.23%. Found: C, 45.76; H, 3.38; N, 2.12%.

IR (ATR, cm<sup>-1</sup>): 3086 (m)  $\nu$ (C–H); 1677 (s)  $\nu$ (C=O); 1469 (s)  $\nu$ (C=C); 1424 (m)  $\delta$ (C–H); 650 (m)  $\nu$ (C–S); 541 (w)  $\nu$ (C–I); 457 (w)  $\nu$ (S–S).

### X-ray crystallography

Crystal data and refinement details for **1-3** are collated in Table 1. Intensity data for colourless crystals of **1** (0.03 x 0.07 x 0.13 mm), **2** (0.06 x 0.09 x 0.12 mm) and **3** (0.03 x 0.05 x 0.20 mm) were measured at 100 K on a Rigaku/Oxford Diffraction XtaLAB Synergy diffractometer (Dualflex, AtlasS2) fitted with CuK $\alpha$  radiation ( $\lambda = 1.54184 \text{ \AA}$ ) so that 100% data completeness was achieved at  $\theta = 67.7^\circ$ . Data processing and Gaussian absorption corrections were accomplished with CrysAlis Pro.<sup>57</sup> The structures were solved by dual space direct methods using ShelXT<sup>58</sup> and each refinement was by full-matrix least squares on  $F^2$  with anisotropic displacement parameters for all non-hydrogen atoms.<sup>59</sup> The C-bound hydrogen atoms were placed on stereochemical grounds and refined with fixed geometries while the O-bound hydrogen atoms were located from a difference map and refined with O–H =  $0.84 \pm 0.01 \text{ \AA}$ . A weighting scheme of the form  $w = 1/[\sigma^2(F_o^2) + (aP)^2 + bP]$ , where  $P = (F_o^2 + 2F_c^2)/3$ , was introduced in each case. Owing to poor agreement, one reflection, *i.e.* (-6 -5 3), was omitted from the final cycles of refinement of **1**. The programs WinGX,<sup>60</sup> ORTEP-3 for Windows,<sup>60</sup> PLATON<sup>61</sup> and DIAMOND<sup>62</sup> were also employed in the study.

**Table 1** Crystal data and refinement details for the crystals of **1-3**<sup>a</sup>

Compound	<b>1</b>	<b>2</b>	<b>3</b>
X	Cl	Br	I
Molecular weight	535.99	580.45	627.44
<i>a</i> (Å)	7.4730(1)	7.4632(1)	7.4540(1)
<i>b</i> (Å)	7.6103(2)	7.6243(1)	7.6771(1)
<i>c</i> (Å)	21.7932(4)	21.9289(4)	22.1343(2)
$\alpha$ (°)	94.377(2)	94.304(1)	93.932(1)
$\beta$ (°)	100.099(2)	99.668(1)	98.393(1)
$\gamma$ (°)	97.933(2)	97.860(1)	97.715(1)
<i>V</i> (Å <sup>3</sup> )	1202.10(4)	1212.36(3)	1236.70(3)
<i>D</i> <sub>x</sub> (g cm <sup>-3</sup> )	1.481	1.590	1.685
<i>F</i> (000)	556	592	628
$\mu$ (mm <sup>-1</sup> )	3.436	4.324	12.147
no. reflections	17234	30664	60109
no. unique reflections	4966	5088	5159
no. reflections with $I \geq 2\sigma(I)$	4677	4918	5039
<i>R</i> (obs. data)	0.029	0.027	0.026
<i>a</i> and <i>b</i> in weighting scheme	0.036; 0.612	0.029; 1.314	0.044; 1.348
<i>R</i> <sub>w</sub> (all data)	0.075	0.070	0.070
Max. and min. residual peaks (e Å <sup>-3</sup> )	0.31; -0.33	0.39; -0.57	0.50; -0.79

a The three-component crystals have the common composition  $C_{14}H_{10}O_4S_2$ ,  $C_7H_5XO_2$ ,  $C_3H_7NO$  and crystallised in the triclinic space group  $P\bar{1}$  with  $Z = 2$

### Computational studies

The analysis of isostructurality was achieved through various computational studies. Among these, molecular packing analysis was performed using two different software packages, namely *Mercury*<sup>63</sup> and *CrystalCMP*.<sup>64,65</sup> The former approach is based on analysing differences in interatomic distances to calculate the positional differences between a cluster of representative molecules.<sup>66</sup> In the calculation, a cluster size of 15 molecules in each of **1-3** was subjected to a similarity analysis with the criteria being that only molecules within a 20% tolerance for both distances and angles were included in the calculation while molecules with a variation >20% were discarded. Allowance was made for differences in molecular structures, e.g. halide, and inversions were enabled during the analysis. As for the latter approach, the similarity is calculated based on the differences between the relative positions and rotations of molecules in a representative cluster.<sup>64</sup> In the present study, the analysis was conducted by setting DTBA as the central molecule with all non-hydrogen atoms in the molecule being selected for overlapping within a cluster size of 10 molecules. Default parameters were applied in the packing similarity calculations.

The Hirshfeld surface analysis was performed through *CrystalExplorer17*<sup>67</sup> following methods as reported in the literature.<sup>68</sup> Briefly, the corresponding crystal structures were used as input with all X–H bond length being adjusted to their neutron-derived values.<sup>69</sup> The interaction energy calculations were performed using the dispersion-corrected CE-B3LYP/6-31G(*d,p*) model as available in *CrystalExplorer17*,<sup>67</sup> with the total intermolecular energy being the sum of energies of four main components comprising electrostatic, polarisation, dispersion and exchange-repulsion with scale factors of 1.057, 0.740, 0.871 and 0.618, respectively.<sup>70</sup> The

model was validated with considerable accuracy against the B3LYP-D2/6-31G(*d,p*) counterpoise corrected energy model as well as the benchmark CCSD(T)/CBS model.<sup>71</sup> The energy frameworks for **1-3** were computed for a cluster of  $2 \times 2 \times 1$  unit-cells with the energy cut-off being set to 8 kJ/mol. Finally, the total energy was obtained for a cluster of molecules within a 25 Å radius from a selected reference molecule employing the same level of theory and basis set model as specified above. The lattice energies for **1-3** were calculated using equation (1),<sup>72</sup> where the second term is the cell dipole energy correction, with  $\rho_{\text{cell}}$  being the vector sum of the molecular dipole moments,  $V_{\text{cell}}$  being the volume and  $Z$  being the number of formula units in the unit-cell. Typically, the cell dipole energy correction is negligible (< 1.00 kJ/mol) for unit-cells with small dipole moments.<sup>73</sup>

$$E_{\text{lattice}} = \frac{1}{2} \sum_{R_{AB} < R} E_{\text{total}}^{\text{AB}} - \frac{2\pi\rho_{\text{cell}}^2}{3ZV_{\text{cell}}} \quad (1)$$

The molecular electrostatic mapping (MEP) were also performed on the individual components comprising **1-3** that had been geometry-optimised using the DFT-B3LYP<sup>74</sup> approach coupled with Ahlrichs's valence triple-zeta polarization basis set ( $\omega$ B97XD/def2-TZVP)<sup>75,76</sup> as available in *Gaussian16*;<sup>77</sup> the results were processed and visualised in *GaussView6*.<sup>79</sup> The choice of the hybrid B3LYP functional was governed by the observation that this level of theory performs well for the geometry optimisation of molecules, while the range-separated  $\omega$ B97XD functional was chosen for the calculation of properties and energies owing to its relatively good accuracy.<sup>79</sup>

In order to calculate an estimate of the energy of stabilisation provided by the C–X⋯quasi- $\pi$ [{⋯HOC=O}<sub>2</sub>] interactions, the experimental three-molecule aggregates encompassing these were evaluated after correction for the basis set superposition error through the counterpoise method,<sup>80,81</sup> as available in *Gaussian16*,<sup>77</sup> with the long-range corrected  $\omega$ B97XD DFT-functional<sup>82</sup> coupled with the Ahlrichs's valence triple-zeta polarization basis set.<sup>75</sup>

## Results and discussion

The mechano-grinding of the precursors, *viz.* DTBA.DMF and 4-halogenated benzoic acids, in the presence of a few drops DMF afforded binary co-crystal solvates **1-3**. The PXRD patterns measured at room temperature on the bulk sample were matches for the calculated PXRD patterns from the CIF's, ESI† Figure 1. In order to determine the source of the DMF, *i.e.* from the DTBA.DMF co-former itself or from the DMF solvent employed in the crystallisation, several grinding experiments were conducted, as shown in ESI† Figure 2. Initially, PXRD were recorded on physical mixtures comprising the co-formers of each of **1-3**. Rietveld analysis indicated 1:1 mixtures of co-formers. Grinding experiments were conducted in the absence of solvent. Rietveld analysis indicated the formation of **1-3** but only in small yields, namely 4, 8 and 3%, respectively. With liquid-assisted grinding (DMF), the yields of **1-3** rose considerably to 64, 77 and 32%, respectively. These results are consistent with the source of the DMF in **1-3** being from the crystallisation from solvent.

The binary co-crystal solvates were subjected to TGA and DSC analyses in order to determine their thermal behaviour; thermal traces are given in ESI† Figure 3. The thermal processes are similar to each other and are rather straightforward and are exemplified by **1**. For **1**, the first step involved the liberation of DMF with the onset temperature being 116.8°C, accounting for 9.1% weight loss *cf.* calculated weight loss of 13.7%. The second stage of decomposition corresponded to the loss of the 4-chlorobenzoic acid with an onset temperature of 182.6°C (weight loss = 29.1% *cf.* calculated, 29.3%). The third and final stage involved the decomposition of DTBA, starting at 301.5 °C with a weight loss of 56.7% (*cf.* calculated, 57.3%), leaving about 5.1% indeterminate residue. The DSC measurements were conducted in the range -150 to 80 °C, *i.e.* below the temperatures at which the DMF was released from each of **1-3**, and did not display any features, ESI† Figure 4. Finally, **1-3** were investigated

thermo-microscopically. As per the images in ESI† Figure 5, desolvation events with loss of transparency commenced at 143, 211 and 215 °C for **1-3**, respectively, followed by melting at 162, 284 and 267 °C, respectively.

### **Molecular structures of 1-3**

The constituents of binary co-crystal solvate **1** are shown in Fig. 1(a); see ESI† Figure 6 for molecular structure diagrams of **2** and **3**. A 1:1:1 ratio of DTBA, 4-CIBA and DMF comprise the asymmetric-unit of **1**, each molecule on a general position; definitive assignments for the presence of carboxylic acid residues is seen in the patterns of C–O bond lengths (ESI† Table 1). As expected, the DTBA molecule<sup>13,14</sup> is twisted about the S1–S2 bond with the C14–S1–S2–C15 torsion angle being  $-94.48(6)^\circ$ . The dihedral angle between the phenyl rings of  $77.81(5)^\circ$  indicates a near to orthogonal disposition. The dihedral angles between the planes through carboxylic acid-(C8,O3,O4) residue and the phenyl ring to which it is connected is  $16.04(11)^\circ$  and along with the analogous angle between (C21,O5,O6)/(C15-C20) of  $13.29(8)^\circ$  indicate twists in the molecule. This contrasts the decidedly smaller (C1,O1,O2)/(C2-C7) angle noted in 4-CIBA, *i.e.*  $4.88(9)^\circ$ .

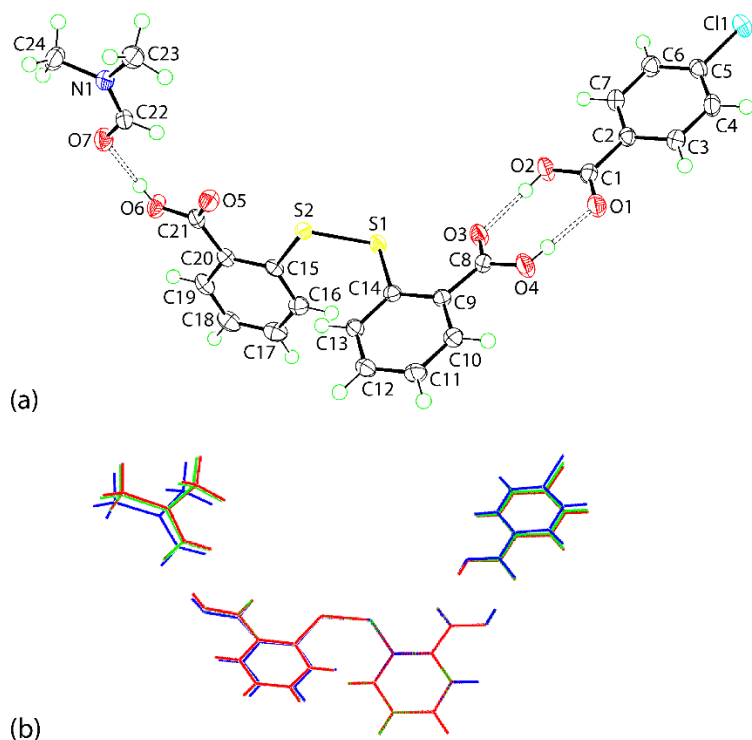


**Fig. 1** (a) The molecular structures of the constituents of binary co-crystal solvate crystal **1** showing atom-labelling scheme and displacement ellipsoids at the 70% probability level; the numbering schemes for **2** and **3** mimic that for **1**. Dashed lines indicate conventional hydrogen bonds. (b) An overlay diagram for the constituents of **1** (red image), **2** (green) and **3** (blue). The molecules have been superimposed so the C9, C11 and C13 atoms are coincident.

The molecules in **2** and **3** resemble closely that described for **1**. From the data included in ESI† Table 1 and the overlay diagram of Fig. 2(b), it is evident there is a high degree of concordance between **1-3** with variations in key conformational parameters being no more than 3° across the series.

### Molecular packing

Conventional hydrogen bonding interactions play a pivotal role in connecting the independent molecules of **1**, Fig. 1(a). Thus, the 4-CIBA and DBTA molecules assemble *via* a non-symmetric, eight-membered  $\{\cdots\text{HOC}=\text{O}\}_2$  synthon; geometric parameters characterising the

intermolecular interactions are given in Table 2. The second carboxylic acid of DTBA forms a hydroxyl-O–H $\cdots$ O(carbonyl) bond with the DMF molecule with a short, reciprocating DMF-C–H $\cdots$ O(carbonyl) contact; the same description obviously pertains to the association in **2** and **3**; data are summarised in ESI† Table 2.

**Table 2** A summary of the geometric parameters (Å, °) characterising the key intermolecular contacts in the crystal of **1**

Contact	H $\cdots$ B	A $\cdots$ B	A–H $\cdots$ B	Symmetry operation
O2–H2o $\cdots$ O3	1.799(17)	2.6452(15)	177(2)	$x, y, z$
O4–H4o $\cdots$ O1	1.786(16)	2.6132(15)	172(2)	$x, y, z$
O6–H6o $\cdots$ O7	1.742(17)	2.5764(15)	176(2)	$x, y, z$
C22–H22 $\cdots$ O5	2.37	3.1256(17)	137	$x, y, z$
C13–H13 $\cdots$ O7	2.57	3.3313(17)	138	$1-x, 1-y, 2-z$
C11–H11 $\cdots$ S1	2.80	3.4732(14)	128	$x, -1+y, z$
C22–O7 $\cdots$ Cg(C15-C20)	3.8926(12)	3.5355(15)	64.31(8)	$1-x, 1-y, 2-z$
C24–H24b $\cdots$ Cg(C15-C20)	2.82	3.5158(16)	128	$1-x, 1-y, 2-z$
Cg(C2-C7) $\cdots$ Cg(C9-C14)	–	3.7340(8)	6.20(6)	$1-x, 1-y, -z$
Cg(C2-C7) $\cdots$ Cg(C2-C7)	–	3.8326(8)	0	$2-x, 2-y, -z$
C17–H17 $\cdots$ Cg(C9-C14)	2.83	3.7738(16)	174	$-1+x, y, z$

A rather large number of non-covalent interactions were identified in the crystal, based on geometric criteria,<sup>61</sup> which serve to link the three-molecule aggregates of **1** into a three-dimensional architecture; geometric data describing these are also included in Table 2. The presence of DTBA-C–H $\cdots$ O(DMF) contacts link centrosymmetrically related three-molecule

aggregates and these are connected in turn, *via* translational symmetry along the *b*-axis, by DTBA-C–H···S(DTBA) interactions to form a supramolecular tape, Fig. 2(a). Also featuring within the tape are interactions of the type DMF-O··· $\pi$ (DTBA-phenyl), within centrosymmetrically-related aggregates, and DMF-C–H··· $\pi$ (DTBA-phenyl), between translationally-related aggregates. For the former, the DMF-carbonyl group approaches the DTBA-phenyl ring in a parallel fashion with the carbonyl-O atom atop the ring centroid and the carbonyl-C atom atop the phenyl-C11 atom, being separated by 3.786(2) Å. The connections between tapes, highlighted in the unit-cell diagram of Fig. 2(b), are of the type  $\pi$ (4-CIBA-phenyl)··· $\pi$ (DTBA-phenyl),  $\pi$ (4-CIBA-phenyl)··· $\pi$ (4-CIBA-phenyl) and DTBA-C–H··· $\pi$ (DTBA-phenyl).

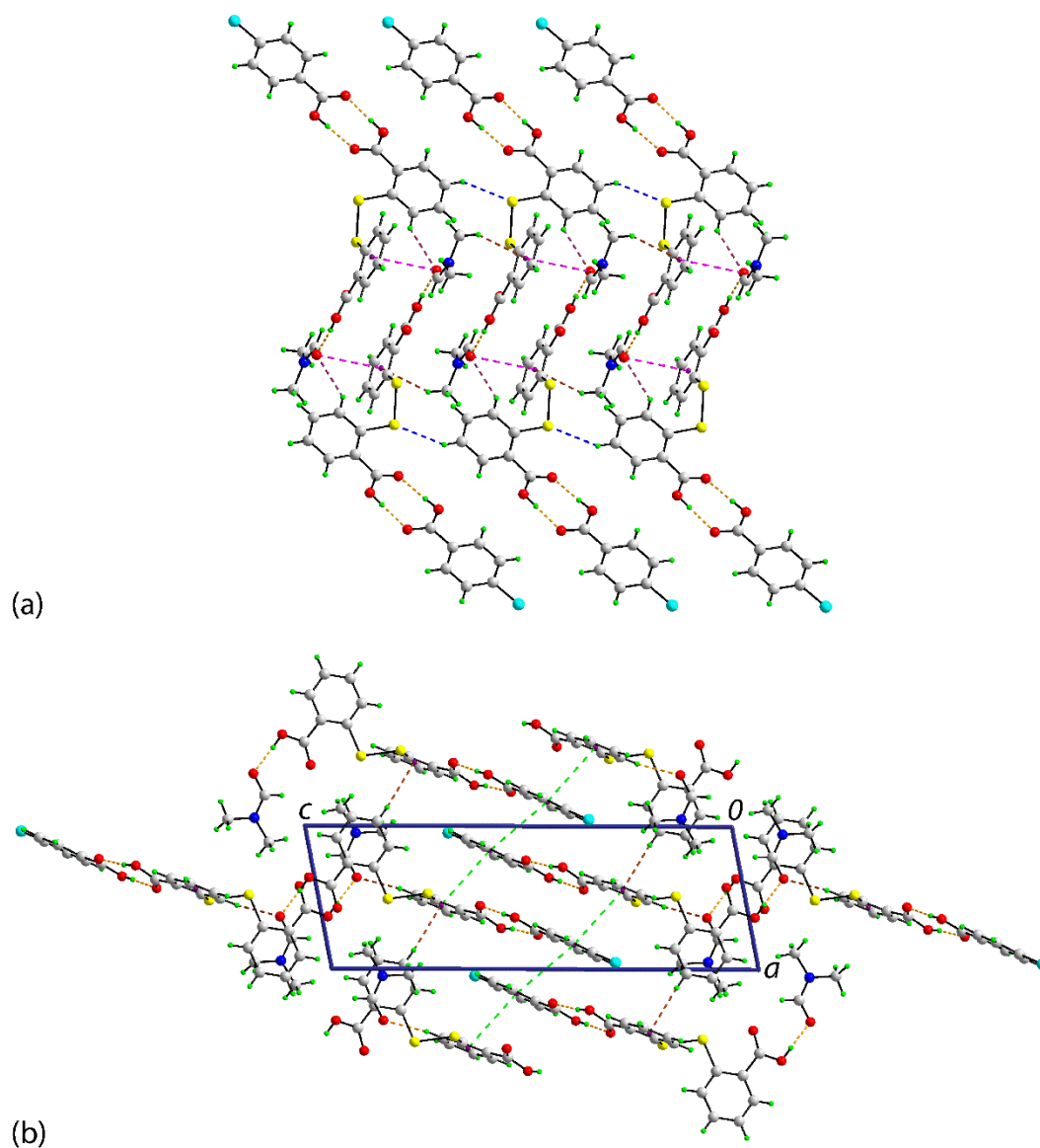


**Fig. 2** Images of the molecular packing in **1**: (a) supramolecular aggregation leading to a tape along the *b*-axis and (b) view of the unit-cell contents in projection down the *b*-axis. The intermolecular contacts are represented by dashed lines: O–H···O (red), C–H···S (blue), C–H···O (plum), C–H··· $\pi$  (brown), C–O··· $\pi$  (pink) and  $\pi$ ··· $\pi$ (green).

The nature and pattern of the points of contact identified above for **1** are replicated in the crystal of **2** as detailed in ESI† Table 2. However, differences occur in the crystal of **3**. The DTBA-C17–H··· $\pi$ (DTBA-phenyl) contact between tapes in **1** and **2** is lacking in **3**, seemingly being directly replaced by DMF-H···O(DTBA-carbonyl) and DTBA-C–

H $\cdots$ S(DTBA) contacts. Further, an additional 4-**I**BA-H $\cdots$ O(DTBA-hydroxyl) contact is evident within the supramolecular tape. Geometric details and diagrams for interactions in the crystal of **3** are given in ESI $\dagger$  Table 2 and Figure 7, respectively.

### **Molecular electrostatic potential (MEP) mapping**

The molecules of DTBA, DMF, 4-**C**IBA, 4-**Br**BA and 4**I**-BA extracted from the crystals of **1-3** were subjected to molecular electrostatic potential (MEP) mapping in order to comprehend the electrostatic charge properties of the individual components in the crystals and correlate these with their intermolecular interactions. Not surprisingly, the mapping results for the constituents of **1-3** are similar to each other and differ primarily in the magnitudes of the calculated charges, therefore only the results for **1** are shown in Fig. 3 while those of **2** and **3** are shown in ESI $\dagger$  Figure 8.

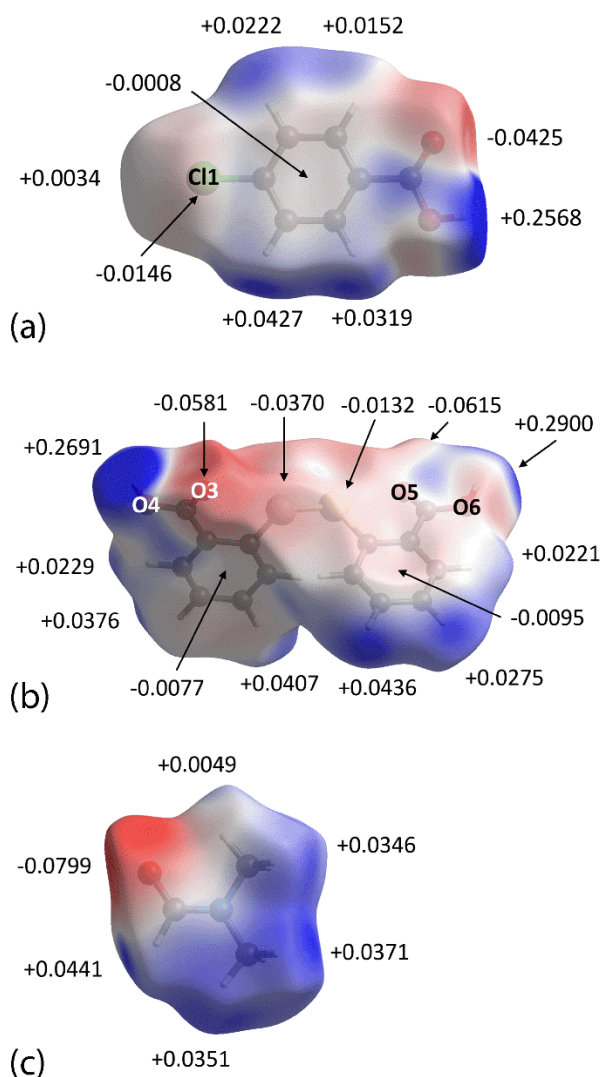


**Fig. 3** The MEP mapped on the Hirshfeld surface of **1**: (a) 4-CIB, (b) DTBA and (c) DMF showing the electrostatic potential charge on selected atoms.

The greatest electrostatic negative charges are localised on DMF-O7 (-0.0799 a.u. for **1** to -0.0807 a.u. for **3**), DTBA-O5 (-0.0615 a.u. for **1** to -0.0622 a.u. for **2**), DTBA-O3 (-0.0579 a.u. for **2** to -0.0585 a.u. for **3**) as well as 4-XBA-O1 (-0.0425 a.u. for **1** to -0.0427 a.u. for **3**). These observations are counter-balanced by the electrostatic positive charges of the acidic hydrogen atoms, *i.e.* DTBA-H6o (+0.2900 for **1** to +0.2906 a.u. for **2**), DTBA-H4o (+0.2688 for **3** to +0.2700 a.u. for **2**), for 4-XBA-H2o (+0.2557 a.u. for **2** to +0.2568 a.u. for **1**) and DMF-H22 (+0.0441 a.u. for **1** to +0.0448 for **2**), thereby leading to complementary electrostatic

attractions between the donor and acceptor atoms. No systematic trends are apparent in the cited electrostatic charges calculated for the experimental structures but it is noted the differences are rather small.

The relatively high electronegative charge for DMF-O7 is likely to be the main reason contributing to its competitive interaction with DTBA-H6o, leading to the consistent formation of the binary co-crystal solvates in this study.

The influence of the halide substituents upon the MEP mapping appears to be minimal with the notable but expected variations in the electrostatic charges about the X atoms. Thus, there is gradual increment of electrostatic positive charges at the sigma hole of X across the series in the order of Cl (+0.0034 a.u.) < Br (+0.0129 a.u.) < I (+0.0216 a.u.); despite this variation it is not sufficiently significant to induce any halogen bonding interactions in the crystals. Systematic variations are also noted in the electrostatic negative charge on the perimeter of the halide atoms in the order Cl (-0.0146 a.u.) > Br (-0.0138 a.u.) > I (-0.0108 a.u.) along with the small increase of charge at the centroid of the respective aromatic ring Cl (-0.0008 a.u.) < Br (-0.0010 a.u.) < I (-0.0015 a.u.) observations due to the reduction of the electron density at the perimeter of the halogen atom as the size of the halide atom increases.<sup>84</sup> The clear influence of molecular packing on the MEP's is apparent when the above results are compared to the MEP's calculated for the geometry-optimised molecules, illustrated in Fig. 4.

The mapping results for the corresponding optimised DTBA (2-fold symmetric) and DMF molecules in **1-3** are identical to each other and therefore, only the results for **1** are discussed along with those of the individual 4-XBA molecules. In accord with the above, the localisation of the maximum negative charges follows the same trends, *i.e.* O7 > O3 = O5 > O1. The differential between the positive charges on the acidic protons is not as marked in the optimised molecules with the charges on H2o in the 4-XBA molecules being marginally greater than that localised on the H4o = H6o atoms. There is a systematic increase of positive charge

on the H<sub>2</sub>O atom from X = Cl to I but, again the differences are small. The influence of the X atom on the MEP mapping is not great but results in systematic trends, unlike for the experimental molecules. The most significant deviation is due to the gradual increment of electrostatic positive charge at the  $\sigma$ -hole in the order of Cl (+0.0073 a.u.) < Br (+0.0141 a.u.) < I (+0.0246 a.u.). Complementing this is the variation of negative charge at the perimeter the C–X bond, *i.e.* Cl (-0.0111 a.u.) < Br (-0.0117 a.u.) < I (-0.0123 a.u.).

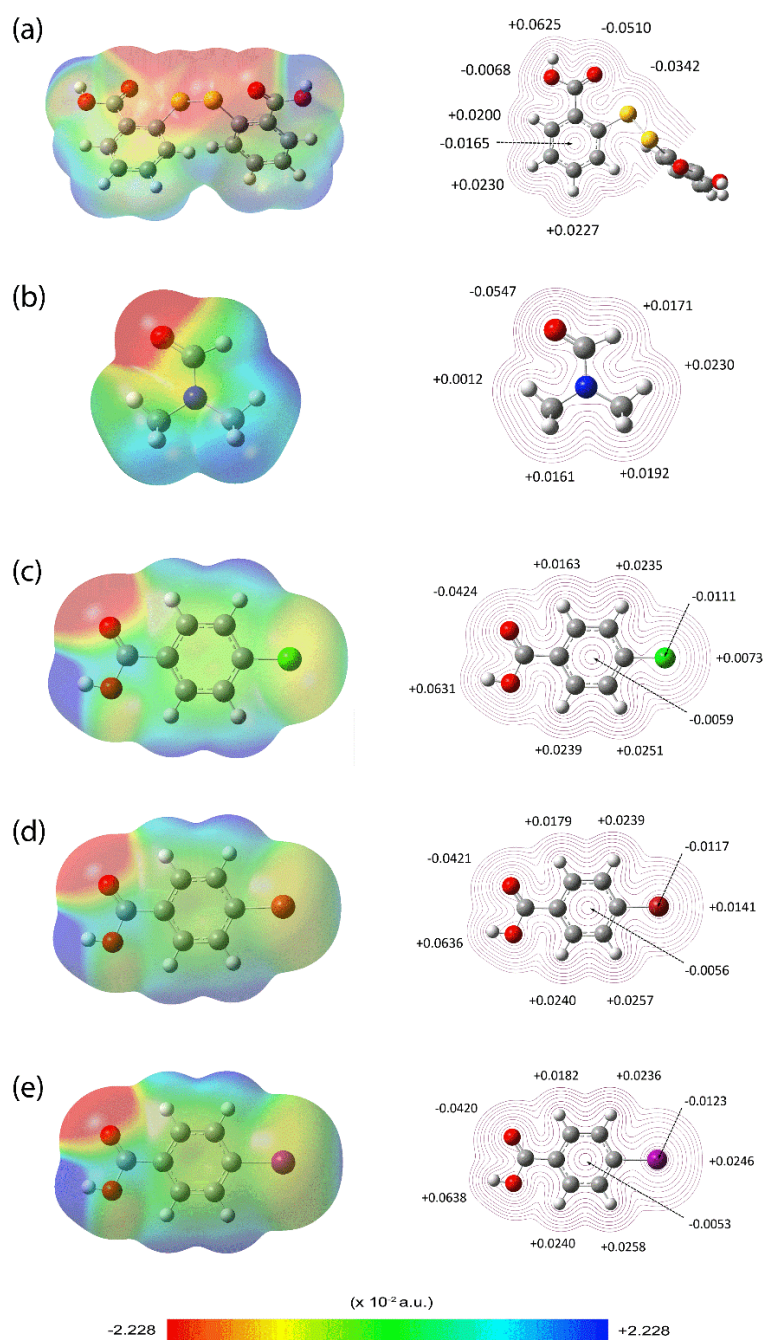


**Fig. 4** The MEP maps and two-dimensional contour plots (iso-density = 0.004 a.u.) for geometry-optimised (a) DTBA, (b) DMF, (c) 4-CIBA, (d) 4-BrBA and (e) 4-IBA, showing the electrostatic potential charge on selected atoms.

### Isostructurality analysis

The molecular packing similarity was performed using two approaches. In the first approach, employing *Mercury*,<sup>63</sup> the results show the crystals have very similar molecular packing as evident from the complete overlay of all molecules (15 out of 15) of the studied clusters with the r.m.s. deviations between **1** and **2**, **1** and **3** as well as **2** and **3** being 0.049, 0.157 and 0.111 Å, respectively; ESI† Figure 9. In the second approach, through *CrystalCMP*,<sup>64,65</sup> the fitting of molecules within the defined cluster results in the dendrogram (ESI† Figure 10) demonstrate there are zero non-overlapped molecules in the comparisons between **1** and **2** as well as between **1** and **3** as indicated by the dark-green dendrogram,<sup>64</sup> while the similarity matrix shows that **1** and **2**, **1** and **3** as well as **2** and **3** have indices of 0.0757, 0.3068 and 0.2254, respectively, *i.e.* conforming to the trend of r.m.s. deviations obtained using *Mercury*. The results verify that the molecular packings of **1**, **2** and **3** are close to identical and therefore, substantiates the isomorphous relationship between these crystals.

### Hirshfeld surface analysis

Having established the isomorphous relationship between crystals **1-3**, the individual components comprising the asymmetric-unit were subjected to a Hirshfeld surface analysis in order to gain better insight into the nature of interactions involving these molecules, in particular to discern any trends that can be traced to the influence of the halide atoms. The mapping of the normalised contact distance ( $d_{\text{norm}}$ ) on the iso-density surfaces of the individual components reveal several red spots of variable intensity indicating the presence of close

contacts which are shorter than the sum of van der Waals radii.<sup>69</sup> The  $d_{\text{norm}}$ -mapping for **1-3** present essentially the same features and hence, discussion will focus upon **1**. The most intense red spots signifying the shortest contact distances are attributed to the hydroxyl-O–H $\cdots$ O(carbonyl) hydrogen bonds which involve all individual components, Fig. 5 and ESI† Figure 11. Apart from the interactions identified through PLATON,<sup>61</sup> the Hirshfeld surface analysis also revealed other close C–H $\cdots$ O and C–H $\cdots$ C contacts as listed in Table 3. These are intra-tape 4-XBA-C6–H $\cdots$ O1(carbonyl, 4-XBA) and DTBA-C10–H $\cdots$ O2(4-XBA, hydroxyl) contacts. The other additional contact, *i.e.* DTBA-C19–H $\cdots$ C19 occurs between tapes.

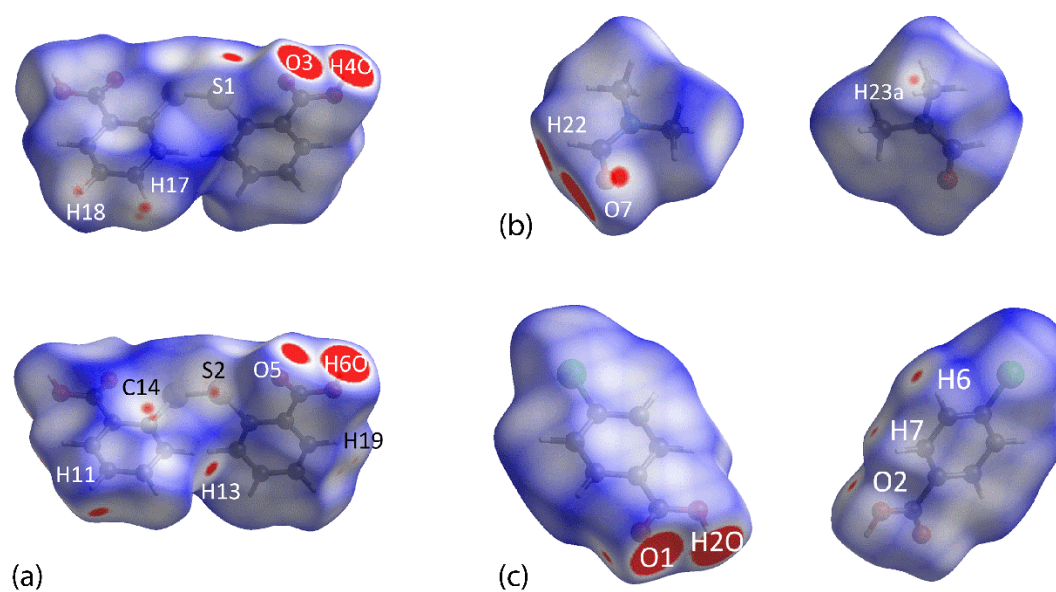


**Fig. 5.** Perspective views of  $d_{\text{norm}}$ -mappings within the property range of -0.0595 to 1.0429 arbitrary units for the individual components of **1**: (a) DTBA, (b) DMF and (c) 4-CIBA.

**Table 3** Listing of the  $d_{\text{norm}}$  contact distances (adjusted to neutron values) for all interactions present in **1-3** in comparison to the corresponding sum of van der Waals radii ( $\Sigma\text{vdW}$ ).

Contact (X–Y⋯Z)	Distance (Å)			$\Sigma\text{vdW}$ (Å)	Symmetry operation
	1	2	3		
O2–H2o⋯O3	1.66	1.67	1.67	2.61	$x, y, z$
O4–H4o⋯O1	1.64	1.64	1.63	2.61	$x, y, z$
O6–H6o⋯O7	1.60	1.59	1.59	2.61	$x, y, z$
C22–H22⋯O5	2.27	2.29	2.31	2.61	$x, y, z$
C13–H13⋯O7	2.47	2.48	2.49 <sup>a</sup>	2.61	$1-x, 1-y, 1-z$
C11–H11⋯S1	2.72	2.71	2.69	2.89	$x, -1+y, z$
C6–H6⋯O1	2.50	2.49	2.50	2.61	$x, 1+y, z$
C10–H10⋯O2	2.51	2.52	2.52	2.61	$x, -1+y, z$
C19–H19⋯C19	2.76	2.78	2.79 <sup>b</sup>	2.79	$-x, 1-y, 1-z$
C17–H17⋯C14	2.72	2.73	2.79	2.79	$-1+x, y, z$
C17–H17⋯C13	2.74	2.76	2.81	2.79	$-1+x, y, z$
C7–H7⋯O4	2.54	2.52	2.50	2.61	$x, 1+y, z$
C18–H18⋯S2	2.83	2.81	2.78	2.89	$-1+x, y, z$
C23–H23b⋯O5	2.55	2.52 <sup>c</sup>	2.49 <sup>d</sup>	2.61	$2-x, 2-y, 1-z$

<sup>a</sup>  $1-x, 1-y, 2-z$ ; <sup>b</sup>  $-x, 1-y, 2-z$ ; <sup>c</sup> C23–H23c⋯O5,  $-x, -y, 1-z$ ; <sup>d</sup>  $2-x, 2-y, 2-z$

The most obvious variations on the  $d_{\text{norm}}$  maps calculated for **1-3** are related to the presence of diminutive red spots associated with the C17–H17⋯C13, C14 contacts, arising from the C17–H17⋯ $\pi$ (C9-C14) interactions in **1** and **2** but are absent for **3**, as the contact distance is at or beyond the van der Waals radii separation; see ESI† Figure 12. However, the C7–H7⋯O4, C18–H18⋯S2 and C23–H23b⋯O5 contacts noted above in the conventional

analysis of the molecular packing of **3**, ESI† Table 2, but absent in **1** and **2**, are not apparent, indicating their weak nature.

Further analysis on the contact distances listed in Table 3 suggest a few conclusions. Before doing so, it is noted that while correlating small variations in distances involving intrinsically weak intermolecular contacts can be perilous,<sup>84,85</sup> in the present case, each crystal structure determination was performed under identical experimental conditions and are isomorphous, perhaps enhancing confidence in comparisons between geometric parameters.<sup>86,87</sup> In terms of the conventional hydrogen bonds linking the components of the asymmetric-unit, only small variations in the separations are apparent, *i.e.* no more than  $\pm 0.01$  Å, indicating the robustness of the three-molecule aggregate in each of **1-3**. Variations are evident in the three other contacts common to the three crystals, *i.e.* C22–H $\cdots$ O5 (+0.04 Å from **1** to **3**), C13–H $\cdots$ O7 (+0.02 Å) and C11–H $\cdots$ S1 (-0.03 Å). Of the additional three contacts identified from the Hirshfeld surface analysis, the C6–H $\cdots$ O1 and C10–H $\cdots$ O2 contacts vary little ( $\pm 0.01$  Å from **1** to **3**), but the other contacts gradually increase in length, passing from **1** to **3**, *i.e.* C19–H $\cdots$ C19 (2.76 to 2.79 Å).

Particularly gratifying in this analysis are the systematic variations in the separations between the identified contacts that differentiate the packing of **1** and **2**, and that of **3**. Thus, the C–H $\cdots$  $\pi$  contact present in **1** and **2** but absent in **3**, manifested in the C17–H $\cdots$ C14, C13 separations, increase in length by 0.07 Å from **1** to **3**. Conversely, the contacts identified in **3** but absent in each of **1** and **2**, *i.e.* C7–H $\cdots$ O4, C18–H $\cdots$ S2 and C23–H $\cdots$ O5 decrease in length by 0.04, 0.05 and 0.06 Å, respectively.

It is also instructive to evaluate the changes in the unit-cell edges among the isomorphous crystals. There is a small contraction in the length of the *a*-axis passing from **1** to **2**, *i.e.* -0.01 Å, and from **2** to **3**, *i.e.* -0.01 Å, Table 1. By contrast, elongations are noted in the *b*- (+0.01 Å for **1** to **2** and +0.06 Å for **2** to **3**) and, especially, *c*-axes (+0.14 and +0.20 Å).

The elongation along the *b*- and *c*-axes is readily traced to the increasing size of the halide atom, Fig. 2(b). Thus, when viewed in projection down the *c*-axis it is apparent the halide lies on the unit-cell edge, *a*. The chemical substitution has the effect of pushing the supramolecular tapes apart, to the extent of diminishing the influence of the DTBA-C17–H··· $\pi$ (DTBA-phenyl) contact in **3** and at the same time enabling the greater significance of the DMF-C23–H···O(DTBA-carbonyl) and DTBA-C18–H···S2(DTBA) contacts. Further support for this hypothesis is the decrease in the length of the *a*-axis along which the aforementioned interactions occur.

Further Hirshfeld surface analysis of the nature of intermolecular interactions along this direction, namely *via* the curvedness, Fig. 6(a), and shape index, Fig. 6(b), mappings, points to the influence of close interactions between of the respective halide atom with the quasi  $\pi$ -hole of the  $\{\cdots\text{HOC}=\text{O}\}_2$  synthon giving rise to a centrosymmetric dimer, Fig. 6(c); analogous images for **2** and **3** are shown in ESI† Figure 12. The ability of  $\{\cdots\text{HOC}=\text{O}\}_2$  synthons to participate in intermolecular interactions analogous to those formed by arene rings, while comparatively rare, are documented in the literature,<sup>88,89</sup> having aromatic character,<sup>90,91</sup> as is the ability of halide atoms to participate in interactions with arene rings,<sup>92-95</sup> including side-on approaches.<sup>95-97</sup>

In **1-3**, the X···ring centroid separations increase with the nature of the halide, Cl (3.36 Å) < Br (3.39 Å) < I (3.50 Å). The halide approaches the ring in a side-on fashion, as manifested in the C–X···Cg angles of 95.1, 93.7 and 90.1°, respectively, for X = Cl to I, and consistent with X(lone-pair)··· $\pi$  interactions. As X is approximately plumb to the ring centroid, the interaction can be considered “delocalised”.<sup>98</sup> Relative to the respective van der Waals radii of X, *i.e.* 1.75, 1.85 and 1.98 Å,<sup>71,99</sup> the C–Cl···quasi- $\pi$  $\{\cdots\text{HOC}=\text{O}\}_2$  interactions increase in significance from Cl < I, also consistent with the shortening of the *a*-axis. As shown in the non-covalent interaction (NCI) plot for **1** in Fig. 6(d), the C–Cl···quasi- $\pi$  $\{\cdots\text{OCOH}\}_2$

interaction is attractive and not merely a result of the more conventional  $\pi(\text{C2-C7})\cdots\pi(\text{C2-C7})$  interaction (see below); analogous NCI plots for **2** and **3** are given in ESI† Figure 13.

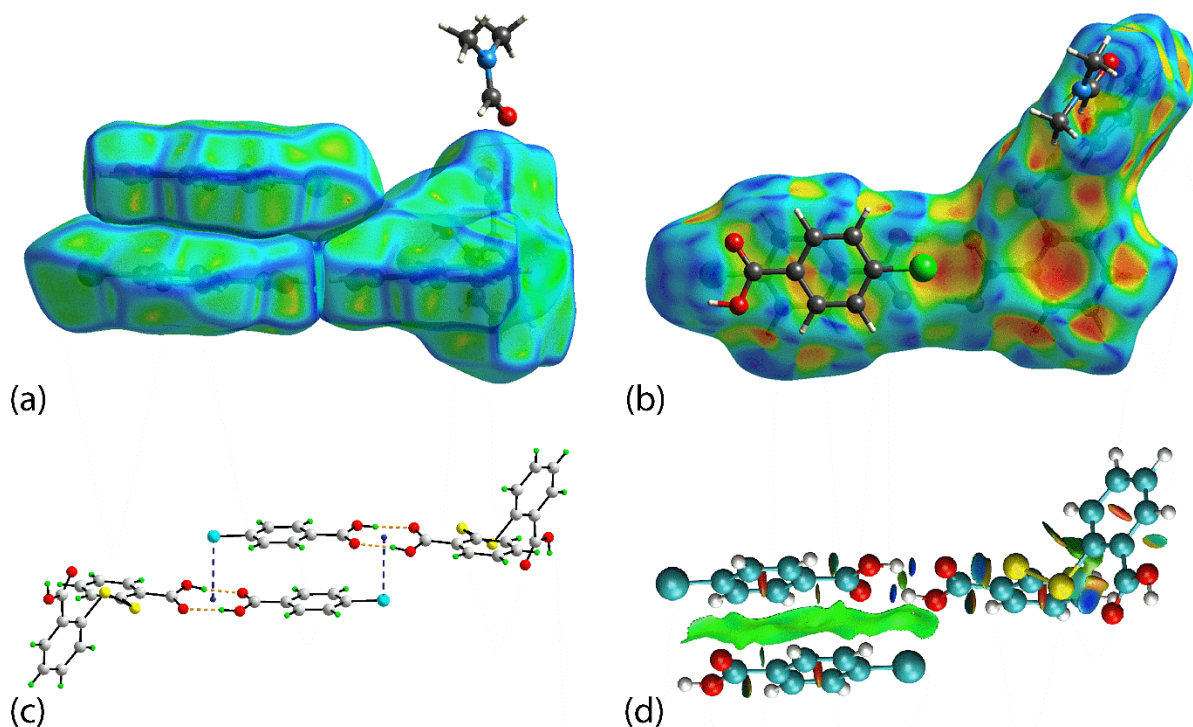


**Fig. 6.** The Hirshfeld surface mapped with (a) curvedness (property range:  $-4.0$  to  $+0.4$  arbitrary units; left) and (b) shape index (property range:  $-1.0$  to  $+1.0$  arbitrary units; right) for **1**, showing the shape complementarity between the quasi  $\pi$ -hole of  $\{\cdots\text{HOC}=\text{O}\}_2$  and Cl. (c) The centrosymmetric dimer featuring  $\text{C}-\text{Cl}\cdots\text{quasi-}\pi[\{\cdots\text{HOC}=\text{O}\}_2]$  interactions in the crystal of **1**; symmetry operation:  $2-x, 2-y, 1-z$  and (d) non-covalent interaction (NCI) plot showing the iso-surface of the reduced density gradient resulting from the  $\text{C}-\text{Cl}\cdots\text{quasi-}\pi[\{\cdots\text{HOC}=\text{O}\}_2]$  interaction in **1**. The iso-surface is coloured according to the values of electron density, with green indicative of weak attraction, while blue and red are indicative of strong attraction and strong repulsion, respectively. The cut-off value is set at  $\text{RDG} = 0.5$  a.u. and colour scale is within  $-0.4 < \rho < 0.4$  a.u.

The quantification of surface contacts in the packing of **1-3** was performed by combining the  $d_i$  and  $d_e$  contact distances at intervals of 0.01 Å to calculate the two-dimensional fingerprint plots for the respective components in the co-crystals: the overall and decomposed profiles delineated into specific contacts, *i.e.* H···H, H···O/O···H, H···C/C···H and H···S/S···H, are presented in ESI† Figure 14 with results summarised in Figure 15. In addition, through the partition of the decomposed contact surfaces between pairs of interacting species, the enrichment ratios for all identified close surface contacts were also calculated to assess the propensity for the formation of specific intermolecular interactions,<sup>100</sup> data are also included in ESI† Figure 15.

As might be expected for the isomorphous crystals, the two-dimensional fingerprint plots for each set of the individual components of **1-3** show very similar characteristics. The calculated Hirshfeld surface contacts for the DTBA molecules are dominated by H···H (28.8%) > H···O/O···H (26.1–26.3%) > H···C/C···H (17.0–17.1%) > H···S/S···H (12.9–13.6%) > C···C (4.4–4.7%) > H···X/X···H (2.1–2.2%) > other minor contacts. The greatest variation of 0.7% in the distribution of contacts is noted for H···S/S···H while the rest vary by no more 0.3%. This observation may reflect the greater influence of the DTBA-C18–H···S2(DTBA) interaction in the packing of **3**. Among the specified close contacts, only the H···O/O···H, H···C/C···H and H···S/S···H contacts result in separations less than the sum of the respective van der Waals radii, based on the shortest  $d_i + d_e$  distances tipped at, respectively, *ca* 1.58–1.66, 2.72–2.80 and 2.70–2.82 Å. The enrichment ratios for the H···O/O···H, H···S/S···H and C···C contacts have values of 1.4, 1.6 and 1.9, respectively, *i.e.* all greater than the unity, indicating these contacts are favoured in the packing as compared to those contacts with a ratio less than 1.<sup>101</sup>

The majority of the close contacts for the DMF molecules in **1-3** are dominated by H···H (45.2–46.2%), H···O/ O···H (23.7–24.0%) and H···C/ C···H (15.1–15.4%) contacts

along with minor contributions from H $\cdots$ X (4.1–4.7%), H $\cdots$ S/S $\cdots$ H (2.7–3.0%) and C $\cdots$ C (2.0–2.1%) contacts. The enrichment ratios for the H $\cdots$ O/O $\cdots$ H, H $\cdots$ X, H $\cdots$ S/S $\cdots$ H and C $\cdots$ C close contacts have relatively high propensity to form, even though only the H $\cdots$ O/O $\cdots$ H contacts occur at distances less than the sum of the van der Waals radii. The H $\cdots$ O/O $\cdots$ H contacts exhibit a pair of asymmetric fang-like peaks in the decomposed fingerprint profiles, with the peak attributed to (internal)-H $\cdots$ O-(external) tipped at *ca* 2.28–2.30 Å, while the other peak ascribable to (internal)-O $\cdots$ H-(external) is tipped at *ca* 1.58–1.60 Å. Worthy of special mention are the relatively high contributions of H $\cdots$ O contacts to the Hirshfeld surfaces. The deviation between the (high) enrichment ratios and (long) contact distances could be due to the relatively large exposed surfaces of the interacting atoms. A closer inspection of the H $\cdots$ X surface contacts suggests some of these arise owing to relatively close DMF-C $\cdots$ X interactions, suggestive of weak tetrel bonding.<sup>101</sup> The non-covalent interaction plots for **3**, Fig. 7, and for **1** and **2**, ESI Figure 16, show these interactions are attractive and qualitatively increase for X = Cl < Br < I. Thus, the C24 $\cdots$ X separations (sum of the van der Waals radii<sup>61,99</sup>) for **1** to **3**, *i.e.* 3.4933(16) (3.45 Å), 3.552(2) Å (3.55 Å) and 3.659(3) Å (3.68 Å), indicate a more significant interaction in **3**; symmetry operation:  $x, y, -1+z$ .

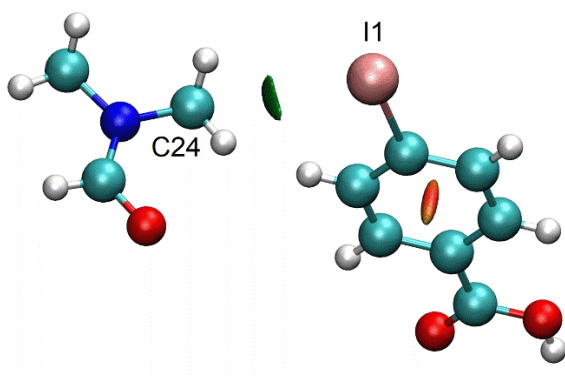


**Fig. 7.** Non-covalent interaction (NCI) plot showing the iso-surface of the reduced density gradient resulting from DMF-C $\cdots$ I interaction in **3**. The iso-surface is coloured according to the values of electron density, with green indicative of weak attraction, while blue and red are

indicative of strong attraction and strong repulsion, respectively. The cut-off value is set at  $\text{RDG} = 0.5$  a.u. and colour scale is within  $-0.4 < \rho < 0.4$  a.u.

A change is noted in the nature of the Hirshfeld surface contacts for 4-**XBA** in that the major contacts are of the type  $\text{H}\cdots\text{O}/\text{O}\cdots\text{H}$  (26.9–28.5%) followed by  $\text{H}\cdots\text{H}$  (25.2–26.6%),  $\text{H}\cdots\text{X}/\text{X}\cdots\text{H}$  (16.1–19.1%),  $\text{C}\cdots\text{C}$  (11.9–13.1%) and  $\text{H}\cdots\text{C}/\text{C}\cdots\text{H}$  (6.7–7.5%) contacts; only the  $\text{H}\cdots\text{O}/\text{O}\cdots\text{H}$  contacts display relatively short  $d_i + d_e$  distances in the range 1.63–1.67 Å. Generally, the decomposed fingerprint plots of those major contacts feature a symmetrical pattern indicating an equal distribution between the (internal)-Y $\cdots$ Z-(external) and (internal)-Z $\cdots$ Y-(external) contacts. The exception occurs for  $\text{H}\cdots\text{X}/\text{X}\cdots\text{H}$  whereby the distribution is predominantly focussed upon (internal)-X $\cdots$ H-(external) (14.8–17.9% vs 1.1–1.3%) suggesting that the contact is heterogenous in nature, *i.e.* the halide atoms are inclined towards interactions with other molecules rather than with symmetry-related 4-**XBA** molecules. In terms of the enrichment ratio, the  $\text{H}\cdots\text{O}/\text{O}\cdots\text{H}$  contacts are enhanced consistent with the short  $d_i + d_e$  contact distances;  $\text{C}\cdots\text{C}$  and  $\text{H}\cdots\text{X}/\text{X}\cdots\text{H}$  contacts also enhanced but at relatively long  $d_i + d_e$  distances.

### Calculation of interaction energies

The pairwise interactions present in the crystals of **1-3** were subjected to energy calculations whereby the  $E_{\text{electrostatic}}$ ,  $E_{\text{polarization}}$ ,  $E_{\text{dispersion}}$  and  $E_{\text{repulsion}}$  terms were computed and summed to give  $E_{\text{total}}$ .<sup>66</sup> Data for the individual energy terms are collated in ESI† Table 3 while Table 4 lists the  $E_{\text{total}}$  values.

**Table 4**  $E_{\text{total}}$  energies (kJ/mol) for identified close contacts present in the crystals of **1-3**.

Contact	<b>1</b>	<b>2</b>	<b>3</b>
O2–H2o···O3 +	-70.9	-71.5	-73.2
O4–H4o···O1			
O6–H6o···O7 +	-59.9	-58.9	-59.9
C22–H22···O5			
C13–H13···O7	-23.9	-23.7	-23.6
C11–H11···S1 +	-12.6	-12.4	-12.4
C11–H11···O3			
$\pi(\text{C2-C7})\cdots\pi(\text{C9-C14})$	-18.4	-19.4	-20.2
$\pi(\text{C2-C7})\cdots\pi(\text{C2-C7})$	-29.6	-30.4	-31.3
C6–H6···O1	-12.2	-12.9	-13.7
C10–H10···O2 +	-6.1	-6.6	-6.7
C7–H7···O4			
C19–H19···C19	-7.5	-7.9	-8.1
C18–H18···S2 +	-16.7	-16.6	-15.6
C17–H17···C13 +			
C17–H17···C14			
C23–H23c···O5	-14.0	-13.7	-13.5
C24···X	-3.7	-4.0	-3.8

As expected, the eight-membered  $\{\cdots\text{HOC=O}\}_2$  synthon resulting from the interaction between DTBA and 4-**X**BA gives rise to the most stable interaction energies with  $E_{\text{total}}$  in the range -70.9 to -73.2 kJ/mol, results consistent with  $E_{\text{total}}$  values of -69.8 to -73.2 kJ/mol obtained for some closely related analogues.<sup>10,12,18</sup> The most stable synthon is found in **3** and

correlated with the influence of the less electronegative iodide atom. The next most stable synthon is the interaction between DTBA and DMF through the  $\{\cdots\text{OC}=\text{O}\cdots\text{O}=\text{COH}\}$  heterosynthon, with a narrow range of  $E_{\text{total}}$  values (-58.9 to -59.9 kJ/mol). Other interactions common to **1-3** that were identified from the geometric analysis of contacts,<sup>61</sup> exhibit significant interaction energies, *i.e.* DTBA-C13-H $\cdots$ O7(DMF), DTBA-C11-H $\cdots$ S1 (and supporting DTBA-C11-H $\cdots$ O3(DTBA) contact),  $\pi(4\text{-XBA-phenyl})\cdots\pi(\text{DTBA-phenyl})$  and  $\pi(4\text{-XBA-phenyl})\cdots\pi(4\text{-XBA-phenyl})$ . The energy of stabilisation provided by the last two interactions are about 1.7-1.8 kJ/mol greater for **3** than for **1**, again correlating with the electronegativity differences of the halide atoms.

The next three contacts to be discussed were identified from the analysis of the calculated Hirshfeld surfaces, *i.e.* 4-XBA-C6-H $\cdots$ O1(4-XBA), DTBA-C10-H $\cdots$ O2(4-XBA) (and supporting 4-XBA-C7-H $\cdots$ O4(DTBA) contact) and DTBA-C19-H $\cdots$ C19(DTBA), all exhibit a small increase in  $E_{\text{total}}$  in the order X = Cl < Br < I, Table 4.

The reverse trend in energies is noted in the DTBA-C17-H $\cdots$ C13, C14(DTBA) (and supporting DTBA-C18-H $\cdots$ S2) contacts consistent with the elongation of the DTBA-C17-H $\cdots$ Cg(DTBA) separations noted above. Counteracting this is the shortening of the supporting DTBA-C18-H $\cdots$ S2 from **1** to **3**. The other two contacts deemed to be present in **3** but not in **1** and **2**, based on geometric criteria alone, *i.e.* 4-XBA-C7-H $\cdots$ O4(DTBA) (and supporting DTBA-C10-H $\cdots$ O2(4-XBA)) and DMF-C23-H $\cdots$ O5(DTBA), correlate with systematic increases and decreases in  $E_{\text{total}}$ , Table 2. Such small changes in energy are entirely consistent with the perturbation in the molecular packing traced to the influence of the size of the halide atom. Finally, the energies associated with the C24 $\cdots$ X contacts (tetrel bonding) are close to each other with a maximum of -4.0 kJ/mol for **2**.

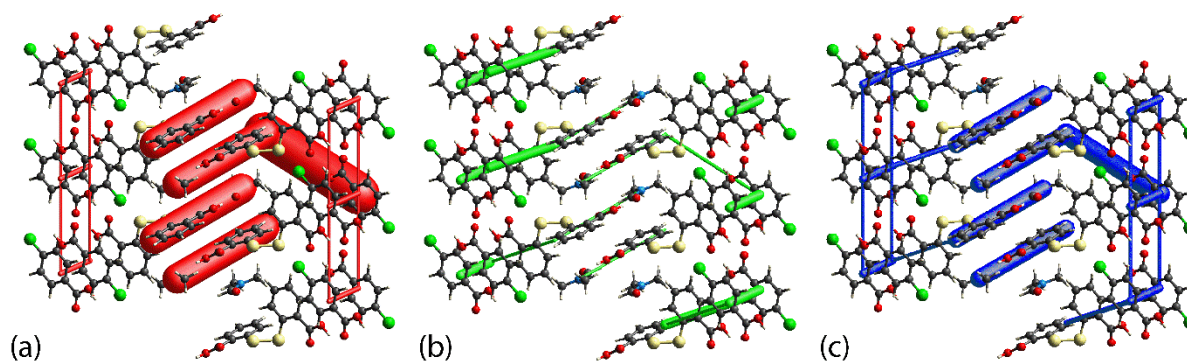
It was also thought of interest to estimate the strength of interaction for C-X $\cdots$ quasi- $\pi(\cdots\text{O1}=\text{C1}-\text{O2}-\text{H2o}\cdots\text{O3}=\text{C8}-\text{O4}-\text{H4o})$  interactions noted above.<sup>75,77,80-82</sup> With reference to

Fig. 6(d), the energy of stabilisation of the three-molecule aggregate for **1** was calculated (-108.7 kJ/mol). This aggregate was then decomposed into the two-molecule aggregates sustained by the hydrogen bonds yielding an energy of stabilisation of 70.9 kJ/mol; similarly, the energy for the  $\pi(\text{arene})\cdots\pi(\text{arene})$  interaction was calculated to be -32.8 kJ/mol. The difference in energy is ascribed to the influence of the  $\text{C}-\text{Cl}\cdots\text{quasi-}\pi(\cdots\text{O1}=\text{C1}-\text{O2}-\text{H2o}\cdots\text{O3}=\text{C8}-\text{O4}-\text{H4o})$  interaction, *i.e.* 2.8 kJ/mol. This energy is less than 3.6 and 5.0 kJ/mol for the X = Br and I derivatives, respectively.

### Energy framework and crystal lattice energy

The simulation of the energy frameworks was performed to further analyse the packing in **1-3**. The isomorphous relationship in the molecular packing is clearly reflected in the similarity of the respective energy frameworks illustrated for **1** in Fig. 8, and in ESI† Figure 17 for **2** and **3**. Overall, the molecular packing of **1** is dominated by electrostatic forces appearing in a zigzag pattern owing to the strong, directional  $\text{O}-\text{H}\cdots\text{O}$  interactions supported by weaker electrostatic forces attributed to  $\text{C}-\text{H}\cdots\text{O}$  interactions that lead to a ladder-like rectangular array co-existing within the framework. The framework due to dispersion forces has a helical form and is mainly sustained by  $\pi\cdots\pi$  interactions that play a limited structure-directing role.

While the energy frameworks for **1-3** resemble each other closely, there is a discernible influence exerted by the 4-halide substituents.<sup>102</sup> This is evident through the quantitative calculation of the lattice energy, which is at a maximum for **3**, being about 8.1 and 16.5 kJ/mol more stable than **2** and **1**, respectively, Table 5. The Kitagorokii packing coefficients<sup>61</sup> of 71.0, 71.1 and 70.8% for **1-3**, respectively, are very close to each other and show no trends.



**Figure 8.** Perspective views of the (a) electrostatic energy, (b) dispersion force and (c) overall energy framework for **1**. The cylindrical radius is proportional to the relative strength of the corresponding energies and adjusted to the same scale factor of 100 with a cut-off value of 8 kJ/mol within a  $2 \times 2 \times 1$  unit-cells.

**Table 5** The lattice energy,  $E_{\text{lattice}}$  (kJ/mol), and the corresponding energy components ( $E_{\text{electrostatic}}$ ,  $E_{\text{polarization}}$ ,  $E_{\text{dispersion}}$  and  $E_{\text{repulsion}}$ ) calculated for a cluster of molecules within 25 Å from the reference molecule through the CE-B3LYP/6-31G(*d,p*) model.

Crystal	$E_{\text{electrostatic}}$	$E_{\text{polarization}}$	$E_{\text{dispersion}}$	$E_{\text{repulsion}}$	$E_{\text{lattice}}$
<b>1</b>	-136.4	-21.5	-64.2	113.3	-108.8
<b>2</b>	-141.5	-21.5	-74.2	120.0	-117.2
<b>3</b>	-146.8	-22.1	-87.0	130.6	-125.3

## Overview

Halogen bonding promotes prominent supramolecular association in crystals containing halides, especially those having the more polarisable iodide atom compared to the lighter congeners, and is well known to be competitive with conventional hydrogen bonding.<sup>103-106</sup> Relevant to the present work is the propensity of organoiodide to interact with the carbonyl-oxygen atom of carboxylic acids. A search of the Cambridge Structural Database,<sup>107</sup> (version

5.42, two updates) was searched for C–I···O=C(OH)R contacts employing ConQuest (version 2.0.4).<sup>108</sup> This resulted in 47 hits out of 296 crystal containing both a carboxylic acid as well as a carbon-bound iodide atom. This hit rate of 16% compares to 10% for crystals with iodide substituted by bromide and nearly 6% for those with chloride. Despite this tendency of organoiodide to disrupt hydrogen bonding, isomorphous relationships can be retained such as in the set of salt hydrates ethacridinium 3-halobenzoate dihydrate (halide = Cl, Br and I) even though I···O interactions are noted but analogous Cl···O and Br···O contacts are not.<sup>46</sup> In a comprehensive evaluation of co-crystals formed between (*N*-5-halopyridin-2-yl)-isonicotinamide/nicotinamide and various aliphatic di-carboxylic acids, it was concluded halogen bonding exhibited by the iodide derivatives precluded isostructural relationships.<sup>51</sup> In **1-3**, despite the steric and bonding effects promoted by the iodide atom, these are not sufficiently significant to promote a change in crystal symmetry.

## Conclusions

In the present series of isomorphous crystals, a dual influence of the larger and more polarisable iodide atom in **3**, as opposed to the chloride (**1**) and bromide (**2**) atoms, is apparent. Firstly, owing to its larger size, the iodide is responsible for the elongation of the *b*- and *c*-axes, which has the result of switching off the DMF–C–H··· $\pi$ (DTBA-phenyl) contact between tapes in **1** and **2**, and replacing these with DMF–H···O(DTBA-carbonyl) and DTBA–C–H···S(DTBA) contacts, absent in **1** and **2**. These interactions along with a more significant C–X···quasi- $\pi$ [{···HOC=O}<sub>2</sub>] bonding interaction in the molecular packing in **3**, compared with those in **1** and **2**, provides a rationale for the contraction of the unit-cell *a*-axis. While the impact of the iodide upon the supramolecular assembly is clear, this influence is accommodated within the crystal symmetry adopted by its lighter congeners, *i.e.* the isomorphous relationship prevails.

### **Conflicts of interest**

The authors declare no competing financial interest.

### **Acknowledgements**

The authors gratefully acknowledge Sunway University Sdn Bhd (Grant numbers GRTIN-IRG-01-2021, GRTIN-IRG-06-2021 and GRTIN-IRG-16-2021) for support of crystallographic studies.

## References

- 1 N. Shan and M. J. Zaworotko, *Drug Discovery Today*, 2008, **13**, 440–446.
- 2 C. B. Aakeröy, J. Desper, M. Fasulo, I. Hussain, B. Levin and N. Schultheiss, *CrystEngComm*, 2008, **10**, 1816–1821.
- 3 C. A. Gunawardana and C. B. Aakeröy, *Chem. Commun.*, 2018, **54**, 14047–14060.
- 4 M. C. Etter, *Acc. Chem. Res.*, 1990, **23**, 120–126.
- 5 G. R. Desiraju, *Angew. Chem. Int. Ed. Engl.*, 1995, **34**, 2311–2327.
- 6 A. S. Cannon and J. C. Warner, *Cryst. Growth Des.*, 2002, **2**, 255–257.
- 7 D. Braga and F. Grepioni, *Chem. Commun.*, 2005, pp. 3635–3645.
- 8 T. R. Shattock, K. K. Arora, P. Vishweshwar and M. J. Zaworotko, *Cryst. Growth Des.*, 2008, **8**, 4533–4545.
- 9 F. H. Allen, W. D. S. Motherwell, P. R. Raithby, G. P. Shields and R. Taylor, *New J. Chem.*, 1999, **23**, 25–34.
- 10 S. L. Tan and E. R. T. Tiekink, *Acta Crystallogr. Sect. E: Cryst. Commun.*, 2020, **76**, 1150–1157.
- 11 Y.-P. Cai, F. Sun, L.-C. Zhu, Q.-Y. Yu and M.-Sh. Liu, *Acta Crystallogr., Sect. E: Struct. Rep. Online*, 2006, **62**, o841–o842.
- 12 S. L. Tan and E. R. T. Tiekink, *Acta Crystallogr., Sect. E: Cryst. Commun.*, 2019, **75**, 475–481.
- 13 G. A. Broker and E. R. T. Tiekink, *CrystEngComm*, 2007, **9**, 1096–1109.
- 14 G. A. Broker, R. P. A. Bettens and E. R. T. Tiekink. *CrystEngComm*, 2008, **10**, 879–887.
- 15 C. E. Rowland, P. M. Cantos, B. H. Toby, M. Frisch, J. R. Deschamps and C. L. Cahill, *Cryst. Growth Des.*, 2011, **11**, 1370–1374.

- 16 L.-L. Wang, H. Chang, E.-C. Yang, *Acta Crystallogr., Sect. C: Cryst. Struct. Commun.*, 2009, **65**, o492–o494.
- 17 H. D. Arman, T. Miller, P. Poplaukhin and E. R. T. Tiekink, *Acta Crystallogr., Sect. E: Struct. Rep. Online*, 2010, **66**, o2592.
- 18 S. L. Tan and E. R. T. Tiekink, *Acta Crystallogr., Sect. E: Cryst. Commun.*, 2019, **75**, 1–7.
- 19 S. L. Tan and E. R. T. Tiekink, *Z. Kristallogr. – New Cryst. Struct.*, 2019, **234**, 1305–1308.
- 20 S. L. Tan and E. R. T. Tiekink, *Z. Kristallogr. – New Cryst. Struct.*, 2019, **234**, 433–436.
- 21 C. R. Groom, I. J. Bruno, M. P. Lightfoot and S. C. Ward, *Acta Crystallogr., Sect. B: Struct. Sci., Cryst. Eng. Mater.*, 2016, **72**, 171–179.
- 22 S. Aitipamula, R. Banerjee, A. K. Bansal, K. Biradha, M. L. Cheney, A. R. Choudhury, G. R. Desiraju, A. G. Dikundwar, R. Dubey, N. Duggirala, P. P. Ghogale, S. Ghosh, P. K. Goswami, N. R. Goud, R. R. K. R. Jetti, P. Karpinski, P. Kaushik, D. Kumar, V. Kumar, B. Moulton, A. Mukherjee, G. Mukherjee, A. S. Myerson, V. Puri, A. Ramanan, T. Rajamannar, C. M. Reddy, N. Rodriguez-Hornedo, R. D. Rogers, T. N. Guru Row, P. Sanphui, N. Shan, G. Shete, A. Singh, C. C. Sun, J. A. Swift, R. Thaimattam, T. S. Thakur, R. K. Thaper, S. P. Thomas, S. Tothadi, V. R. Vangala, N. Variankaval, P. Vishweshwar, D. R. Weyna and M. J. Zaworotko, *Cryst. Growth Des.*, 2012, **12**, 2147–2152.
- 23 E. Grothe, H. Meekes, E. Vlieg, J. H. ter Horst and R. de Gelder, *Cryst. Growth Des.*, 2016, **16**, 3237–3243.
- 24 IUCr, Definition of isomorphous crystals,  
[https://dictionary.iucr.org/Isomorphous\\_crystals](https://dictionary.iucr.org/Isomorphous_crystals).

- 25 IUCr, Definition of isostructural crystals,  
[https://dictionary.iucr.org/Isostructural\\_crystals](https://dictionary.iucr.org/Isostructural_crystals).
- 26 L. Parkanyi, A. Kálmán, S. Sharma, D. M. Nolen and K. H. Pannell, *Inorg. Chem.*, 1994, **33**, 180–182.
- 27 A. Kálmán, *Acta Crystallogr., Sect. B: Struct. Sci., Cryst. Eng. Mater.*, 2005, **61**, 536–547.
- 28 C. M. Reddy, M. T. Kirchner, R. C. Gundakaram, K. A. Padmanabhan and G. R. Desiraju, *Chem. - Eur. J.*, 2006, **12**, 2222–2234.
- 29 D. Cinčić, T. Friščić and W. Jones, *Chem. Mater.*, 2008, **20**, 6623–6626.
- 30 R. Bishop, *Chem. Soc. Rev.*, 1996, **25**, 311–319.
- 31 A. Dey and G. R. Desiraju, *CrystEngComm*, 2004, **6**, 642–646.
- 32 T. Gelbrich, T. L. Threlfall and M. B. Hursthouse, *CrystEngComm*, 2012, **14**, 5454–5464.
- 33 A. K. Jordão, V. F. Ferreira, A. C. Cunha, J. L. Wardell, S. M. S. V. Wardell and E. R. T. Tiekink, *CrystEngComm*, 2012, **14**, 6534–6539.
- 34 S. K. Seth, V. S. Lee, J. Yana, S. M. Zain, A. C. Cunha, V. F. Ferreira, A. K. Jordão, M. C. B. V. de Souza, S. M. S. V. Wardell, J. L. Wardell and E. R. T. Tiekink, *CrystEngComm*, 2015, **17**, 2255–2266.
- 35 O. Shemchuk, D. Braga and F. Grepioni, *Chem. Commun.*, 2016, **52**, 11815–11818.
- 36 I. Giangreco, J. C. Cole and E. Thomas, *Cryst. Growth Des.*, 2017, **17**, 3192–3203.
- 37 P. K. Mondal, R. Shukla, S. Biswas and D. Chopra, *Acta Crystallogr., Sect. B: Struct. Sci., Cryst. Eng. Mater.*, 2018, **74**, 574–591.
- 38 J. F. Gallagher, M. F. Farrell, N. Hehir, P. Mocilac, E. Aubert, E. Espinosa, B. Guillot and C. Jelsch, *Cryst. Growth Des.*, 2019, **19**, 6141–6158.

- 39 B. Bieszczad, S. Pawlędzio, K. Polak, J. Antonowicz, A. Mieczkowski and D. Trzybiński, *CrystEngComm*, 2020, **22**, 5389–5399.
- 40 D. Rosiak, A. Okuniewski and J. Chojnacki, *Acta Crystallogr., Sect. C: Struct. Chem*, 2021, **77**, 11–19.
- 41 P. Bombicz, N. V. May, D. Fegyverneki, A. Saranchimeg and L. Bereczki, *CrystEngComm*, 2020, **22**, 7193–7203.
- 42 S. L. Tan and E. R. T. Tiekink, *CrystEngComm*, 2021, **23**, 1723–1743.
- 43 A. Saïdykhan, N. W. Fenwick, R. D. Bowen, R. Telford and C. C. Seaton, *CrystEngComm*, 2021, **23**, 7108–7117.
- 44 D. Dey and D. Chopra, *Cryst. Growth Des.*, 2017, **17**, 5117–5128.
- 45 I. J. Scowen, T. S. Alomar, T. Munshi and C. C. Seaton, *CrystEngComm*, 2020, **22**, 7334–7340.
- 46 A. Mirocki and A. Sikorski, *Crystals*, 2020, **10**, 79.
- 47 S. Ranjan, R. Devarapalli, S. Kundu, S. Saha, S. Deolka, V. R. Vangala and C. M. Reddy, *IUCrJ*, 2020, **7**, 173–183.
- 48 J. Wojnarska, M. Gryl, T. Seidler and K. M. Stadnicka, *Crystal Growth Des.*, 2020, **20**, 6535–6544.
- 49 M. Roy, K. Li, M. Nisar, L. W.-Y. Wong, H. H.-Y. Sung, R. K. Haynes and I. D. Williams, *Acta Crystallogr., Sect. C: Struct. Chem*, 2021, **77**, 262–270.
- 50 A. M. Petrosyan, G. Giester, V. V. Ghazaryan and M. Fleck, *J. Molec. Struct.*, 2021, **1243**, 130851.
- 51 A. M. Abeysekera, A. S. Sinha and C. B. Aakeroy, *Molecules*, 2021, **26**, 1147.
- 52 G. R. Desiraju, *Angew. Chem. Int. Ed.*, 2007, **46**, 8342–8356.
- 53 D. Cinčić, T. Frišćić and W. Jones, *Chem. – Eur. J.*, 2008, **14**, 747–753.

- 54 L. Xiao, Y. Wu, Z. Yu, Z. Xu, J. Li, Y. Liu, J. Yao and H. Fu, *Chem. – Eur. J.*, 2018, **24**, 1801–1805.
- 55 K. M. Hutchins, K. A. Kummer, R. H. Groeneman, E. W. Reinheimer, M. A. Sinnwell, D. C. Swenson and L. R. MacGillivray, *CrystEngComm*, 2016, **18**, 8354–8357.
- 56 O. Omotoso, D. K. McCarty, S. Hillier and R. Kleeberg, *Clays Clay Miner.*, 2006, **54**, 748–760.
- 57 Rigaku Oxford Diffraction, CrysAlis PRO, Yarnton, Oxfordshire, England (2017).
- 58 G. M. Sheldrick, *Acta Crystallogr., Sect. A: Found. Crystallogr.*, 2008, **64**, 112–122.
- 59 G. M. Sheldrick, *Acta Crystallogr., Sect. C: Struct. Chem.*, 2015, **71**, 3–8.
- 60 L. J. Farrugia, *J. Appl. Crystallogr.*, 2012, **45**, 849–854.
- 61 A. L. Spek, *Acta Crystallogr., Sect. E: Crystallogr. Commun.*, 2020, **76**, 1–11.
- 62 K. Brandenburg, *DIAMOND*, Crystal Impact GbR, Bonn, Germany, 2006.
- 63 C. F. Macrae, P. R. Edgington, P. McCabe, E. Pidcock, G. P. Shields, R. Taylor, M. Towler and J. van de Streek, *J. Appl. Cryst.*, 2006, **39**, 453–457.
- 64 J. Rohlíček, E. Škořepová, M. Babor and J. Čejka, *J. Appl. Cryst.*, 2016, **49**, 2172–2183.
- 65 J. Rohlíček and E. Škořepová, *J. Appl. Cryst.*, 2020, **53**, 841–847.
- 66 J. A. Chisholm and S. Motherwell, *J. Appl. Cryst.*, 2005, **38**, 228–231.
- 67 S. K. Wolff, D. J. Grimwood, J. J. McKinnon, M. J. Turner, D. Jayatilaka and M. A. Spackman, CrystalExplorer (Version 17), University of Western Australia, 2012.
- 68 S. L. Tan, M. M. Jotani and E. R. T. Tiekink, *Acta Crystallogr., Sect. E: Crystallogr. Commun.*, 2019, **75**, 308–318.
- 69 M. A. Spackman and D. Jayatilaka, *CrystEngComm*, 2009, **11**, 19–32.
- 70 C. F. Mackenzie, P. R. Spackman, D. Jayatilaka and M. A. Spackman, *IUCrJ*, 2017, **4**, 575–587.

- 71 M. J. Turner, S. Grabowsky, D. Jayatilaka and M.A. Spackman, *J. Phys. Chem. Lett.*, 2014, **5**, 4249–4255.
- 72 S. P. Thomas, P. R. Spackman, D. Jayatilaka and M. A. Spackman, *J. Chem. Theory Comput.*, 2018, **14**, 1614–1623.
- 73 L. Maschio, B. Civalleri, P. Ugliengo and A. Gavezzotti, *J. Phys. Chem. A*, 2011, **115**, 11179–11186.
- 74 A. D. Becke, *J. Chem. Phys.*, 1993, **98**, 5648–5652.
- 75 F. Weigend and R. Ahlrichs, *Phys. Chem. Chem. Phys.*, 2005, **7**, 3297–3305.
- 76 F. Weigend, *Phys. Chem. Chem. Phys.*, 2006, **8**, 1057–1065.
- 77 M. J. Frisch, G. W. Trucks, H. B. Schlegel, G. E. Scuseria, M. A. Robb, J. R. Cheeseman, G. Scalmani, V. Barone, B. Mennucci, G. A. Petersson, H. Nakatsuji, M. Caricato, X. Li, H. P. Hratchian, A. F. Izmaylov, J. Bloino, G. Zheng, J. L. Sonnenberg, M. Hada, M. Ehara, K. Toyota, R. Fukuda, J. Hasegawa, M. Ishida, T. Nakajima, Y. Honda, O. Kitao, H. Nakai, T. Vreven, J. A. Montgomery, Jr., J. E. Peralta, F. Ogliaro, M. Bearpark, J. J. Heyd, E. Brothers, K. N. Kudin, V. N. Staroverov, R. Kobayashi, J. Normand, K. Raghavachari, A. Rendell, J. C. Burant, S. S. Iyengar, J. Tomasi, M. Cossi, N. Rega, J. M. Millam, M. Klene, J. E. Knox, J. B. Cross, V. Bakken, C. Adamo, J. Jaramillo, R. Gomperts, R. E. Stratmann, O. Yazyev, A. J. Austin, R. Cammi, C. Pomelli, J. W. Ochterski, R. L. Martin, K. Morokuma, V. G. Zakrzewski, G. A. Voth, P. Salvador, J. J. Dannenberg, S. Dapprich, A. D. Daniels, Ö. Farkas, J. B. Foresman, J. V. Ortiz, J. Cioslowski and D. J. Fox, Gaussian 16, Revision C.01, Gaussian, Inc., Wallingford, Connecticut, USA, 2016.
- 78 R. Dennington, T. A. Keith and J. M. Millam, GaussView, Version 6, Semichem Inc., Shawnee Mission, Kansas, USA, 2016.

- 79 É. Brémond, M. Savarese, N. Q. Su, Á. J. Pérez-Jiménez, X. Xu, J. C. Sancho-García and C. Adamo, *J. Chem. Theory Comput.*, 2016, **12**, 459–465.
- 80 S. F. Boys and F. Bernardi, *Mol. Phys.*, 1970, **19**, 553–566.
- 81 S. Simon, M. Duran, and J. J. Dannenberg, *J. Chem. Phys.*, 1996, **105**, 11024–11031.
- 82 J. D. Chai and M. Head-Gordon, *Phys. Chem. Chem. Phys.*, 2008, **10**, 6615–6620.
- 83 A. Friedrich, J. Pahl, J. Eysel, J. Langer, N. V. E. Hommes, A. Görling and S. Harder, *Chem. Sci.*, 2021, **12**, 2410–2418.
- 84 J. D. Dunitz and R. Taylor, *Chem. - Eur. J.*, 1997, **3**, 89–98.
- 85 E. R. T. Tiekink and J. Zukerman-Schpector, *CrystEngComm*, 2009, **11**, 2701–2711.
- 86 K. Kersten, R. Kaur and A. Matzger, *IUCrJ*, 2018, **5**, 124–129.
- 87 P. Sacchi, M. Lusi, A. J. Cruz-Cabeza, E. Nauha and J. Bernstein, *CrystEngComm*, 2020, **22**, 7170–7185.
- 88 H. Karabiyık, H. Karabiyık and N. O. İskeleli, *Acta Crystallogr., Sect. B: Struct. Sci.*, 2012, **68**, 71–79.
- 89 H. Karabiyık, R. Sevinçek and H. Karabiyık, *J. Mol. Struct.*, 2014, **1064**, 135–149.
- 90 M. Palusiak and T. M. Krygowski, *Chem. – Eur. J.*, 2007, **13**, 7996–8006.
- 91 A. Filarowski and I. Majerz, *J. Phys. Chem. A*, 2008, **112**, 3119–3126.
- 92 H. Matter, M. Nazaré, S. Güssregen, D. W. Will, H. Schreuder, A. Bauer, M. Urmann, K. Ritter, M. Wagner and V. Wehner, *Angew. Chem., Int. Ed.*, 2009, **48**, 2911–2916.
- 93 N. K. Shinada, A. G. de Brevern and P. Schmidtke, *J. Med. Chem.*, 2019, **62**, 9341–9356.
- 94 E. Kanao, T. Morinaga, T. Kubo, T. Naito, T. Matsumoto, T. Sano, H. Maki, M. Yan and K. Otsuka, *Chem. Sci.*, 2020, **11**, 409–418.
- 95 E. R. T. Tiekink, *CrystEngComm*, 2021, **23**, 904–928.
- 96 F. Zordan, L. Brammer and P. Sherwood, *J. Am. Chem. Soc.*, 2005, **127**, 5979–5989.

- 97 Y. N. Imai, Y. Inoue, I. Nakanishi and K. Kitaura, *Protein Sci.*, 2008, **17**, 1129–1137.
- 98 D. Schollmeyer, O. V. Shishkin, T. Rühl and M. O. Vysotsky, *CrystEngComm*, 2008, **10**, 715–723.
- 99 A. Bondi, *J. Phys. Chem.*, 1964, **68**, 441–451.
- 100 C. Jelsch, K. Ejsmont and L. Huder, *IUCrJ*, 2014, **1**, 119–128.
- 101 S. Scheiner, *Phys. Chem. Chem. Phys.*, 2021, **23**, 5702–5717.
- 102 K. K. Jha, S. Dutta, V. Kumar and P. Munshi, *CrystEngComm*, 2016, **18**, 8497–8505.
- 103 J. P. M. Lommerse, A. J. Stone, R. Taylor and F. H. Allen, *J. Am. Chem. Soc.*, 1996, **118**, 3108–3116.
- 104 E. Corradi, S. V. Meille, M. T. Messina, P. Metrangolo and G. Resnati, *Angew. Chem. Int. Ed.*, 2000, **39**, 1782–1786.
- 105 A. Mukherjee, S. Tothadi and G. R. Desiraju, *Acc. Chem. Res.*, 2014, **47**, 2514–2524.
- 106 G. Cavallo, P. Metrangolo, R. Milani, T. Pilati, A. Priimagi, G. Resnati and G. Terraneo, *Chem. Rev.*, 2016, **116**, 2478–2601.
- 107 R. Taylor and P. A. Wood, *Chem. Rev.*, 2019, **119**, 9427–9477.
- 108 I. J. Bruno, J. C. Cole, P. R. Edgington, M. Kessler, C. F. Macrae, P. McCabe, J. Pearson and R. Taylor, *Acta Crystallogr., Sect. B: Struct. Sci.*, 2002, **58**, 389–397.